

TRABAJO FINAL DE MASTER

Upconversion luminescence mechanisms in Er^{3+} and $\text{Er}^{3+}/\text{Yb}^{3+}$ doped nanoparticles: dependence on phonon energies and concentrations

Presentado por: Vidal de la Torre González

Realizado en: Universidad de Cantabria

**Bajo la dirección de: Rafael Valiente
Barroso**

Leioa-Santander, septiembre 2023

Table of Contents

1	INTRODUCTION	1
2	THEORETICAL FRAMEWORK	2
2.1	Rare Earths	2
2.2	Free ion approximation	3
2.3	Crystal-field effect	5
2.4	Electronic transitions	5
2.4.1	Radiative transitions. Judd-Ofelt theory	6
2.4.2	Multiphonon relaxation and energy-gap law	6
2.5	Energy transfer	8
2.6	Upconversion mechanisms	8
3	EXPERIMENTAL	10
3.1	Synthesis Methods	10
3.1.1	General Procedures	10
3.1.2	Synthesis of Yttria (Y_2O_3) via homogeneous precipitation	11
3.1.3	Synthesis of YAG ($Y_3Al_5O_{12}$) via Pechini method	11
3.1.4	Synthesis of (YF_3) via hydrothermal method	11
3.2	Characterization techniques	12
3.2.1	X-Ray Diffraction	12
3.2.2	Raman Spectroscopy	12
3.2.3	Diffuse Reflectance Spectroscopy	13
3.2.4	Fluorescence Spectroscopy	13
4	RESULTS AND DISCUSSION	15
4.1	Structural characterization	15
4.2	Spectroscopic characterization	17
4.3	Diffuse Reflectance Spectroscopy	18
4.4	Fluorescence Spectroscopy	20
5	CONCLUSIONS	26

Abstract

Upconversion luminescence, a phenomenon where two or more lower-energy photons are converted into higher-energy emissions, holds significant potential for applications in several fields, including imaging, sensing, security inks, and photonics. Upconversion luminescence mechanisms in Erbium (Er^{3+}) and Erbium-Ytterbium ($\text{Er}^{3+} / \text{Yb}^{3+}$) doped nanoparticles have been investigated, focusing on the influence of dopant concentrations and phonon energies of the host lattice. Through systematic analysis and spectral characterization, we have elucidated how phonon-assisted energy transfers and multiphoton cooperative mechanisms dictate the observed luminescence behavior. Our findings provide valuable insights into tailoring the upconversion efficiency and emission spectra of doped nanoparticles for enhanced applications.

Keywords: Upconversion, luminescence, rare earth ions, nanothermometer.

1 INTRODUCTION

The discovery and development of novel materials have always accompanied technological progress. Nevertheless, the 1960s saying “technology is always limited by the materials available” still holds true today. [1]

Luminescent materials (or phosphors), mostly are solid inorganic materials consisting of a host lattice, usually intentionally doped. The absorption of energy takes place via either the host lattice or on these impurities. In addition, transfer of energy through the lattice can take place. In almost all cases, the emission takes place on intentionally doped impurities, like rare-earth ions, which are present in relatively low concentrations (a few mole percent or less). [2] Most luminescent materials, including organic dyes and Quantum Dots (QDs), follow Stokes law, since they absorb high-energy photons and emit low-energy photons. [3, 4]. On the contrary, upconversion nanophosphors (UCNPs) relate to the conversion of long-wavelength light with lower energy into light with higher energy.

Lanthanide-doped materials exhibit distinctive upconversion luminescence characteristics, such as substantial anti-Stokes shifts spanning hundreds of nanometers, sharp emission lines, extended upconversion luminescence lifetimes, and superior photostability. In early studies, these materials were incorporated into inorganic hosts and were mainly used in lasers, anticounterfeiting applications, and optical devices. [5, 6, 7]

Over the past decade, nanoscale and microscale lanthanide upconversion nanophosphors have been synthesized with controlled size, structure, morphology, and surface ligands. [8, 9] These materials have emerged beyond the well-investigated areas of theranostics and bioanalysis. The latest developments in the application of UCNPs include photomanipulation of membrane-bound proteins, optical tweezers, 3D printing and NIR vision. Other developed applications include molecular switches, lasing, and super-resolution microscopy. [10]

Taking into consideration the present advantages and limitations of upconversion emissive nanophosphors, the future directions of research are oriented towards the optimization of the upconversion efficiency and nanotoxicity and safety assessments. The future directions in the application of Lanthanide UCNPs are therapy applications (photothermal therapy, chemotherapy, photodynamic therapy, photocontrolled release of drugs) or sensing (chemosensors and biosensors). [11]

2 THEORETICAL FRAMEWORK

2.1 Rare Earths

Rare earth (RE) elements constitute a group of 17 elements, which includes the lanthanide series (La, Ce, Pr, Nd, Pm, Sm, Eu, Gd, Tb, Dy, Ho, Er, Tm, Yb, and Lu), along with Y and Sc, as defined by IUPAC. Scandium and yttrium are considered rare earth elements due to the high probability of finding them in the same ore deposits and their similar physicochemical properties. [12]

Despite being named rare earths, they are not rare at all. For instance, Cerium is the 27th most common element of the planet. [13] However, they are extremely difficult to find in pure form, thus the "rare" notation.

Most RE ions (except La and Lu) present partially occupied the $4f$ orbitals. Their electronic configuration goes from La: $[\text{Xe}] (4f^0)5d^16s^2$ to Lu: $[\text{Xe}] 4f^{14}5d^16s^2$. The electronic configuration of RE^{3+} is $[\text{Xe}] 4f^n$, losing the $6s$ and $5d$ electrons. The outer shells ($5s$, $5p$) are completely filled, while the valence electrons are in the $4f$ orbital. This results in a shielding from the crystal environment of the valence electrons, thus barely varying energy levels when introduced in different crystalline host and enabling multiple electronic transitions accompanied by light emission. [14]

Figure 1 shows radial part of the wavefunction as a function the distance associated to atomic orbitals $4f$, $5s$, $6s$ of Gd^+ obtained from Ref. [15].

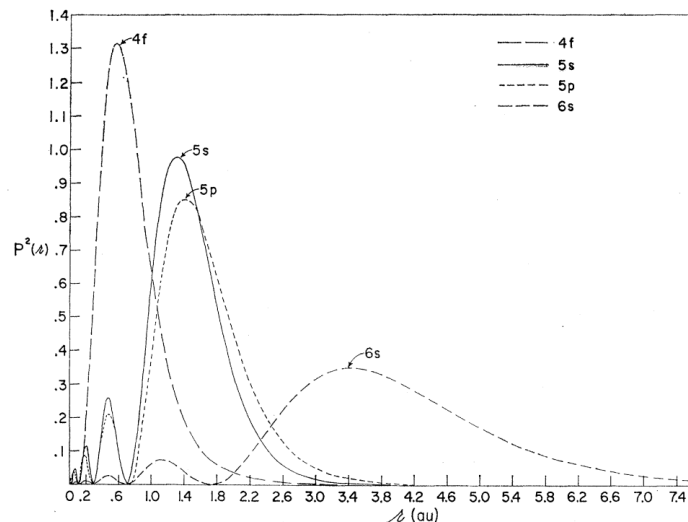


Figure 1: Radial part of the wavefunction as a function the distance associated to atomic orbitals $4f$, $5s$, $6s$ of Gd^+ . [15]

2.2 Free ion approximation

The Hamiltonian that defines the energy levels of electrons in incomplete layers of the free ion, \mathcal{H} , can be expressed as the sum of three terms:

$$\mathcal{H} = H_0 + H_{e-e} + H_{s-o} \quad (1)$$

where H_0 accounts for the kinetic and potential energy of valence electron moving in the spherical field created by the nucleus and filled shells, H_{e-e} describes the interelectronic repulsion between the valence electrons in unfilled shells, and H_{s-o} the spin-orbit interaction. The most relevant, thus the first term to take into account is H_0 . The solutions to this hamiltonian are characterized by quantum numbers n (principal) and l (orbital momentum).

H_{e-e} and H_{s-o} are weaker, but still important. They are both comparable magnitudes and should be considered simultaneously, but the Russell-Saunders approximation allows to treat H_{e-e} before H_{s-o} . H_{e-e} introduces a correction due to the electric field affecting the electron due to other electrons in unfilled shells, so the field will not be spherical any more. By applying the effect of H_{e-e} , total angular momentum \mathbf{L} and total spin \mathbf{S} vectors are introduced to describe the system. Generally, different terms will be labeled by the ^{2S+1}L notation, designating L by a letter (S, P, D, F, G, H...) as a function of its numerical value (0, 1, 2, 3, 4, 5...). The degeneracy now takes the value $(2L+1)(2S+1)$.

The following step is introducing the H_{s-o} interaction, which partially breaks the degeneracy. This term produces the coupling of the \mathbf{L} and \mathbf{S} vectors, which makes them not enough to define the newest levels, so they are not good quantum numbers. That is why their vector sum \mathbf{J} , known as total angular momentum, is introduced:
 $\mathbf{J} = \mathbf{L} + \mathbf{S}$

Finally, the new quantum levels (multiplets) are designed by the $^{2S+1}L_J$ labels, have a $2J+1$ degeneracy, and are energetically separated by a distance proportional to the J value, known as the "Landé interval rule".

The Dieke diagram (Figure 2) shows the energetic positions of states of trivalent rare earths in the LaCl_3 lattice. The energy value at 0 energy corresponds to the ground state, and all other multiplets are excited states. The linewidth of the states indicates the magnitude of the multiplets due to crystal field effect. Additionally, some ions have a semicircle below, indicating that luminescence from these states has been observed.

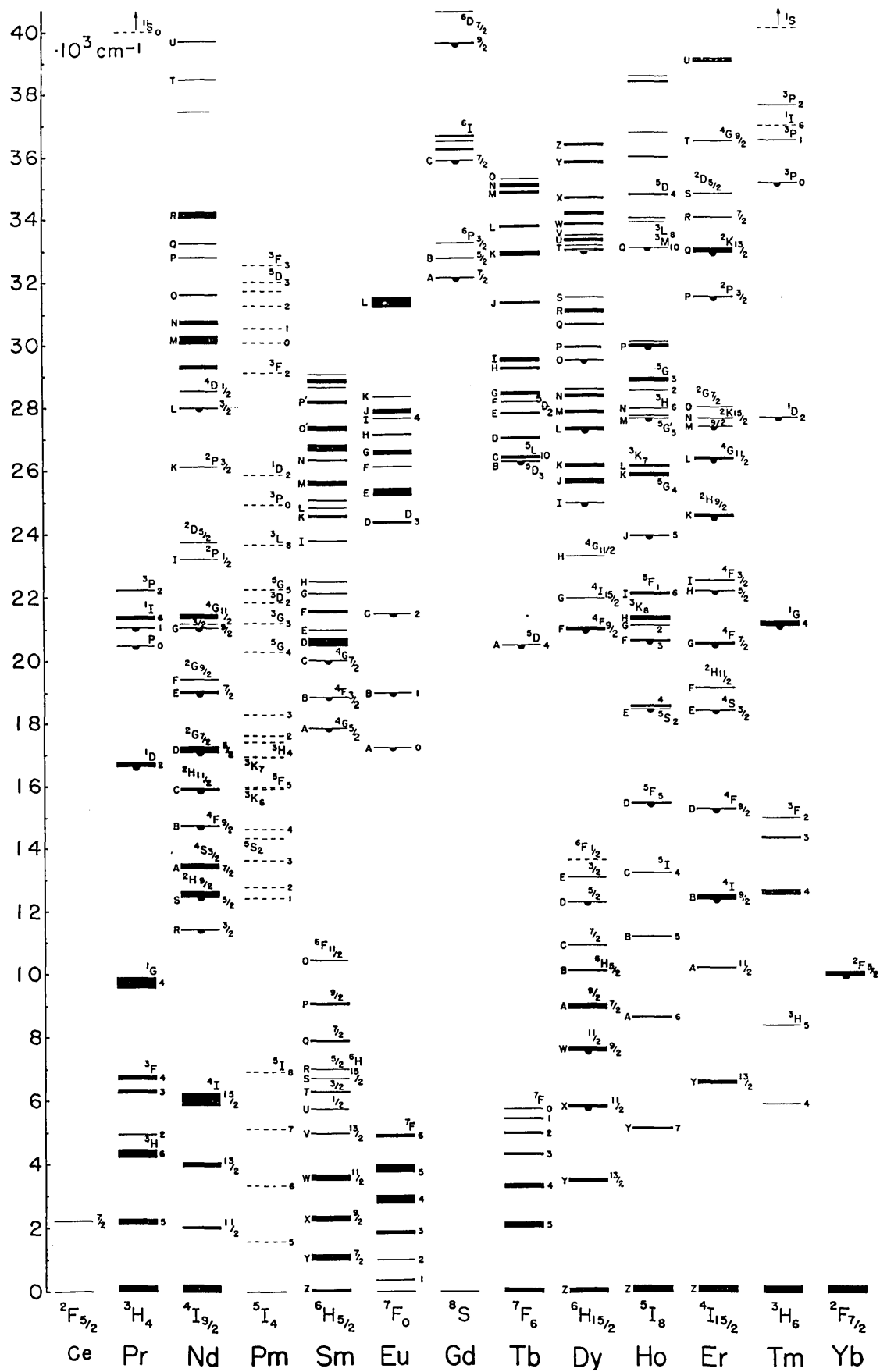


Figure 2: Observed energy levels of the RE³⁺-doped LaCl₃: Dieke Diagram [16]

2.3 Crystal-field effect

When introducing a RE^{3+} ion into a host crystal lattice, the interaction between the lanthanide ion and the neighbour ions (also known as ligands) needs to be taken into account. The charge distribution associated to these ligands will generate an electric field known as the "crystal field", acting on the lanthanide ion. As stated earlier in this theoretical framework, the effect of the crystal field is much weaker than when working with transition metals due to the shielding of the $4f$ orbitals. This effect partially breaks the $2J+1$ degeneracy inversely proportional to the degree of punctual symmetry of the place the ion uses in the material. For RE^{3+} with an odd number of electrons (Kramer ions), the degeneracy can not be completely lifted but using an external magnetic field. Figure 3 shows the effects of different perturbation over the ion.

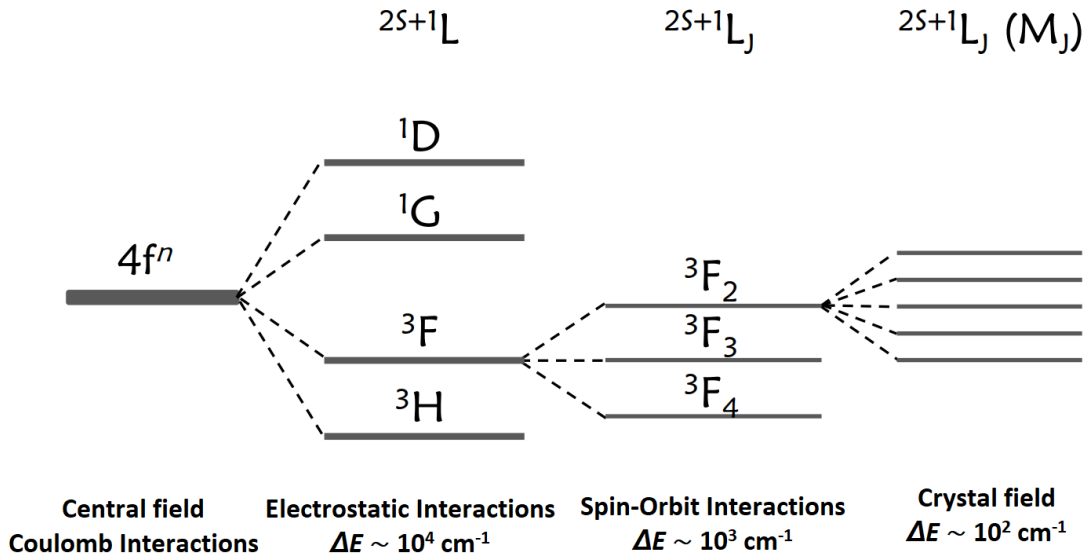


Figure 3: Magnitude of different perturbations on a RE ion. Adapted from Ref. [17]

2.4 Electronic transitions

When an ion goes from an excited state to a lower energy state, the remaining energy can be released via photon emission and/or phonon emission. Electric dipole transitions in lanthanide ions are forbidden due to parity (Laporte Rule). However, emission and absorption associated to these transitions are observed with an intensity higher than the expected from electric quadrupole or magnetic dipole, even though they are allowed. In order to understand this phenomenon, the Judd-Ofelt theory is needed.

2.4.1 Radiative transitions. Judd-Ofelt theory

Judd-Ofelt theory makes the following assumptions:

- The splitting of atomic levels produced by the crystalline field is not considered.
- The energy gap between the fundamental and excited configuration does not depend on the angular momentum J .
- The sublevels that are formed when applying the crystal-field effect are homogeneously populated.
- The host lattice is isotropic

The main conclusion of this theory is that the wave functions of the $4f^n$ levels are mixed with those of the $4f^{n-1}5d^1$ levels or with the charge transfer levels, which enables electrical dipole transitions to be observed as long as the lanthanide is placed in a site without inversion center. It can also be observed if the site is centrosymmetric when there is coupling between the electronic and vibrational wave functions of the lattice through odd vibrational modes. This way the parity of the f - f transitions changes and the transition can be produced through the electric dipole mechanism. In addition to the requirement of having initial and final states with different parity, the new selection rules are as follows:

- $\Delta S = 0$, $\Delta L \leq 6$ if J and $J' \neq 0$
- $\Delta J = 0$ or $\Delta J = 2, 4, 6$ if J and $J' = 0$

If both J and J' were 0, the transition would be forbidden. But even in this case due to Judd-Ofelt, this transition can be observed and it is generally used to determine the number of crystallographic site available for a RE^{3+} . It is the case of Eu^{3+} .

2.4.2 Multiphonon relaxation and energy-gap law

The probability of a (non)radiative emission from an excited energy level of a RE^{3+} ion is strongly related to the energy separation between this level and the level just below it, known as the energy gap (ΔE). Nonradiative transitions predominate between energy levels with a low energy gap, while the opposite is observed for a large energy gap.

Systematic experimental studies performed over different RE^{3+} ions in different host crystals show that the nonradiative emission rate, A_{nr} , from a given energy level decreases exponentially with the corresponding energy gap:

$$A_{nr} = A_{nr}(0) \cdot \exp(-\alpha\Delta E) \quad (2)$$

having $A_{nr}(0)$ and α a strong and weak dependence on the host lattice, respectively.

Figure 4 shows the behaviour of the nonradiative rate as a function of the energy gap for different host lattices. Note the highest phonon energy of each lattice: $\text{LaCl}_3 \approx 250 \text{ cm}^{-1}$, $\text{LaF}_3 \approx 450 \text{ cm}^{-1}$, and $\text{Y}_2\text{O}_3 \approx 700 \text{ cm}^{-1}$.

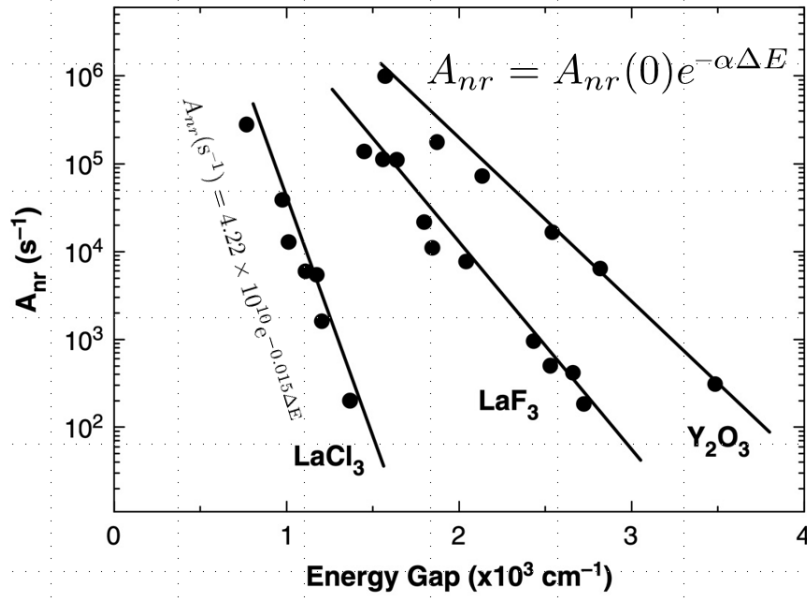


Figure 4: Nonradiative rate as a function of the energy gap for different host lattices. Adapted from Ref. [18]

The exponential decrease in the multiphonon emission rate with an increasing energy gap is due to the increased number of necessary emitted phonons for the transition. The larger the energy gap, the larger is the number of phonons needed to bridge this gap, thus smaller de-excitation probability by multiphonon relaxation.

The phonons that participate in the nonradiative de-excitation processes are the highest-energy phonons with an appreciable density of states (effective phonons).

It is commonly accepted to consider multiphonon relaxation competitive against radiative de-excitation when the energy gap is $6 \hbar\omega_{max}$, with $\hbar\omega_{max}$ the highest energy phonon, and predominant when that relation is smaller.

2.5 Energy transfer

Energy transfer refers to processes by which a previously excited ion (donor or sensitizer) relaxes, either partially or completely, by transferring its energy to a neighboring ion (acceptor or activator), which utilizes it to elevate an electron to a higher energy state.

Energy transfer phenomena do not necessarily result in upconversion emissions. In fact, there are significant energy transfer processes where the emitted photons have the same or lower energy, compared to the exciting photons.

Fermi's golden rule describes the energy transfer rate between the excited donor D^* and the acceptor A :

$$P_{DA} = \frac{2\pi}{\hbar} |\langle \psi_D, \psi_A^* | H_{DA} | \psi_D^*, \psi_A \rangle|^2 \int g_D(E) \cdot g_A(E) dE \quad (3)$$

where ψ denotes the wavefunctions, * an excited state, and H_{DA} the physical interaction leading to the energy transfer. The integral represents the overlap between the normalized donor emission and acceptor absorption shape functions, $g_D(E)$ and $g_A(E)$. Figure 5 graphically shows in pink the overlap between the donor emission and the acceptor absorption shape functions:

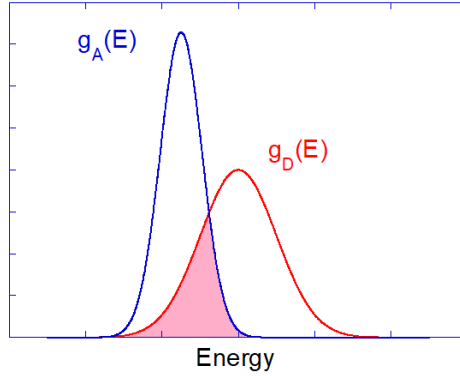


Figure 5: Overlap of emission and absorption shape functions corresponding to spectral overlap integral of equation (2)

2.6 Upconversion mechanisms

There are several mechanisms where low-energy excitation radiation is transformed into higher-energy luminescence. However, not all of these processes constitute upconversion phenomena. Figure 6 shows several of these mechanisms. [19]

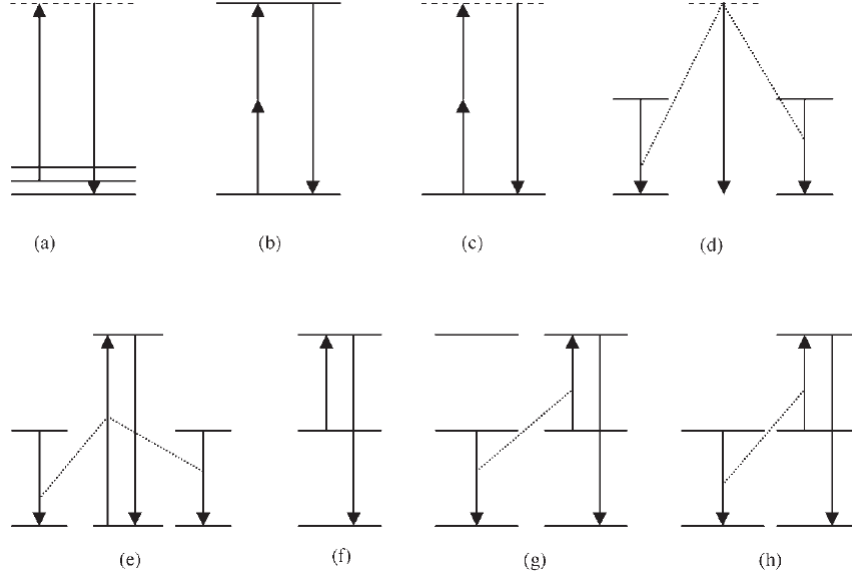


Figure 6: Processes transforming long wavelengths into shorter wavelengths a) Anti-Stokes Raman emission; b) Two Photon Excitation; c) Second Armonic Generation; d) Cooperative Luminescence; e) Cooperative Sensitization; f) Excited State Absorption; g) Energy Transfer Upconversion y h) Sensitized Energy Transfer Upconversion. [19]

Only Excited State Absorption (ESA), where only one ion is needed, and Energy Transfer Upconversion (ETU) and Sensitized Energy Transfer Upconversion (Sensitized ETU), where two or more ions are needed, strictly account for upconversion, since the middle state should be a real state. Any upconversion mechanism requires to absorb energy from the ground state, *Ground State Absorption* (GSA), so ESA and ETU mechanisms are also referred as GSA/ESA and GSA/ETU.

There is an inverse mechanism to ETU, known as Cross-Relaxation (CR), where instead of one ion transferring its excess energy to another, as in ETU, there is a transfer of energy from the higher-energy ion to the lower-energy ion.

In Sensitized ETU, two ions (donors) get excited by absorbing two photons. Then, the energy from these two donors is transferred to a third ion (acceptor), which then emits from a higher energy state. This acceptor does not necessarily have to be close to the donors but must interact through a multipolar mechanism. The energy could travel long distances depending on the donor concentrations, ion distances, and lifetimes.

Since the GSA/ESA process only requires one ion to occur, it predominates with low concentrations, whereas GSA/ETU predominates with higher impurity concentrations. These two mechanisms take place in Er^{3+} and $\text{Er}^{3+}/\text{Yb}^{3+}$ doped materials reported in this thesis.

3 EXPERIMENTAL

Different methods were used to synthesize different RE-doped materials. In addition from the synthesized samples, other samples (NaYF_4 : 20%Yb³⁺, 2%Er³⁺ [20] and SrTiO_3 : 20%Yb³⁺, 2%Er³⁺ [21]) available at the Department of Applied Physics of University of Cantabria were also studied to analyze the effect of high phonon energy of the host material on luminescence properties. Table 1 shows a summary of all the studied samples.

Table 1: Samples summary, notation and synthesis method.

Sample	Lattice	RE Concentration	Synthesis Method
VDG-A	Y ₂ O ₃	20% Yb / 2% Er	Homogeneous precipitation
VDG-B	YAG	20% Yb / 2% Er	Sol-gel Pechini
VDG-C	YF ₃	20% Yb / 0.5% Er	Hydrothermal
VDG-D	YF ₃	20% Yb / 1% Er	Hydrothermal
VDG-E	YF ₃	20% Yb / 2% Er	Hydrothermal
VDG-F	YF ₃	undoped	Hydrothermal
VDG-G	YF ₃	2% Yb / 1% Er	Hydrothermal
VDG-H	YF ₃	5% Yb / 1% Er	Hydrothermal
VDG-I	YF ₃	10% Yb / 1% Er	Hydrothermal
VDG-J	NaYF ₄	20% Yb / 2% Er	Solid State with HF gas flux [20]
VDG-K	SrTiO ₃	20% Yb / 2% Er	Sol-Gel [21]

3.1 Synthesis Methods

3.1.1 General Procedures

Ethanol 96° and deionized water was used. Urea (Assay HPLC: 98.0 - 102%), citric acid (99%), ethylene glycol, ammonium fluoride (96%), aluminum nitrate nonahydrate (99.999%), erbium (III) nitrate pentahydrate (99.9%), yttrium (III) nitrate hexahydrate (99.9%) and ytterbium (III) nitrate pentahydrate (99.9%) were purchased from commercial sources. All chemicals were used without any further purification, and the same precursors were used for all synthesis procedures. All manipulations were performed in air atmosphere.

3.1.2 Synthesis of Yttria (Y_2O_3) via homogeneous precipitation

Yttrium oxide was prepared following the homogeneous precipitation method published for other members of the research group [9]. Briefly, 3 mmol of yttrium including a 20% of ytterbium and a 2% of erbium nitrates were dissolved in a well stirred mixture of 420 mL of deionized water with 1.744 mol of urea. The solution was then heated up at 80°C for 2 h. under stirring. Afterwards, the mixture was naturally cooled down to room temperature and washed with deionized water and centrifuged (4200 rpm x 20 min.) three times. The solid was suspended in ethanol to avoid aggregation, and after being dried at 70 °C, it was calcined at 900°C for 3 h. with a ramp of 5°C/min.

3.1.3 Synthesis of YAG ($\text{Y}_3\text{Al}_5\text{O}_{12}$) via Pechini method

The Pechini method is a variation of the sol-gel method, but using citric acid added to the solvent. The nitrate salts were dissolved in 80 mL of deionized water and citric acid (CA) was then added (molar ratio CA:total cations = 0.1). These metal salts were dissolved at a molar ratio, Y:Al, of 3-x:5, being x a 20% of Yb and a 2% of Er. The mixture was magnetically stirred until a clear solution was obtained. Ethylene glycol (EG) was added into solution at EG:CA molar ratios of 2. The solution was continuously stirred at 80°C in order to facilitate the evaporation of the excess water and accelerate the polyesterification reaction. The gel was then heated up at 100°C in an oven for 24 h. Finally, the gel was calcined at 1200°C for 3 h. in air atmosphere. [22]

3.1.4 Synthesis of (YF_3) via hydrothermal method

Yttrium fluoride with different Er^{3+} and Yb^{3+} concentrations were prepared via hydrothermal method. Briefly, in a typical synthesis 2 mmol of yttrium nitrate including different concentrations of ytterbium and erbium nitrates were dissolved in 70 mL of deionized water. Then, 6 mmol of NH_4F were added to the solution while stirring vigorously at room temperature. HNO_3 or NH_3 was used to adjust the pH of the solutions to 1.7. This final solution was then transferred into a PTFE (Teflon) liner, and placed inside a stainless-steel autoclave reactor and heated up to 180°C for 16 h. with no further heating treatments. The mixture was cooled down to room temperature and washed with deionized water by centrifuging (4200 rpm x 20 min.) three times. The solid was dispersed in ethanol and dried at 70°C.

3.2 Characterization techniques

There are a multitude of existing techniques for the characterization of materials. In this section, only the methods that have been used are shown, considering their relevance and availability when obtaining the desired information about the synthesized samples.

3.2.1 X-Ray Diffraction

X-ray diffraction (XRD) is one of the usual methods for determining the crystalline structure of almost any material. This method provides information about the type of crystalline structure of a sample, as well as the lattice parameter or even the grain size. This is the reason why it was used as a first step before any other method.

A Bruker D8 Advance diffractometer has been used. The X-ray source employed was a sealed copper tube operating at a voltage difference of $V = 40$ kV and a current intensity of $i = 25$ mA, with an average wavelength of $\lambda = 1.54184$ Å. The analysis of the data consisted of conducting a pattern matching with specific software: *Match!* by Crystal Impact, and the *Crystallography Open Database - Inorganics* updated on June 6, 2023.

3.2.2 Raman Spectroscopy

Vibrational spectroscopy is used to study a wide variety of sample types, from solid to gases including liquids, ranging from simple identification to comprehensive quantitative and qualitative analysis of the complete spectrum. Vibrational Raman active bands are characterized by their frequency, intensity, and shape. As vibrational levels are unique to each molecule, Raman spectroscopy serves to identify a specific molecule.

The Raman spectra were obtained using a 514.5 nm laser beam from an Ar⁺-Kr⁺ laser. Then, the dispersed light was passed through a triple monochromator (Horiba-Jobin-Yvon, Model T64000). The two first monochromators are used for filtering the laser line whereas the third one is used for the light analysis. The setup was equipped with a liquid nitrogen-cooled CCD (Charge-Coupled Device) detector.

3.2.3 Diffuse Reflectance Spectroscopy

When handling microcrystalline powdered specimens, direct measurements of absorption or transmittance are unattainable, since light cannot pass through the sample due to scattering. Instead, reflectance spectra can be gathered, which yield analogous insights into the transitions between the material's ground and excited states. The correlation between these two magnitudes can be established through the utilization of the so-called *Kramers-Krönig relations*. [23, 24]

For the determination of diffuse reflectivity under ambient conditions, a Cary 6000i (Varian) spectrophotometer with a Teflon integration sphere was used. It is designed to analyze a wide range of materials, extended from ultraviolet (UV) to visible (Vis) and near-infrared (NIR) wavelengths (from 170 - 1800 nm). Figure 7 shows a scheme of the equipment.

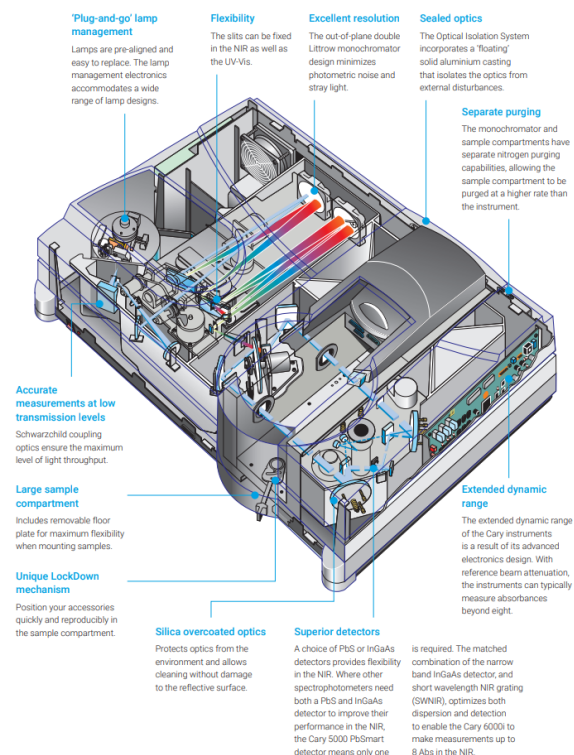


Figure 7: Scheme of the Cary 6000i spectrophotometer

3.2.4 Fluorescence Spectroscopy

Fluorescence spectrometry involves analyzing the photoluminescence of a sample by exciting its electrons with a beam of light of a certain frequency, causing them to emit light at a different frequency.

All emission and excitation spectra, and lifetime measurements were obtained using an Edinburgh Instruments FLSP920 fluorimeter equipped with double monochromators for emission and excitation (Figure 8). The light sources included a continuous 450 W Xenon lamp, a pulsed 60 W Xenon lamp with variable frequencies between 50 and 100 Hz for lifetime measurements, and a tunable 980 nm diode laser ($P_{max} = 5$ W). For emission detection, three distinct electrically cooled photomultiplier tubes were employed, depending on the detection spectral range wavelengths — visible, extended, and near-infrared.

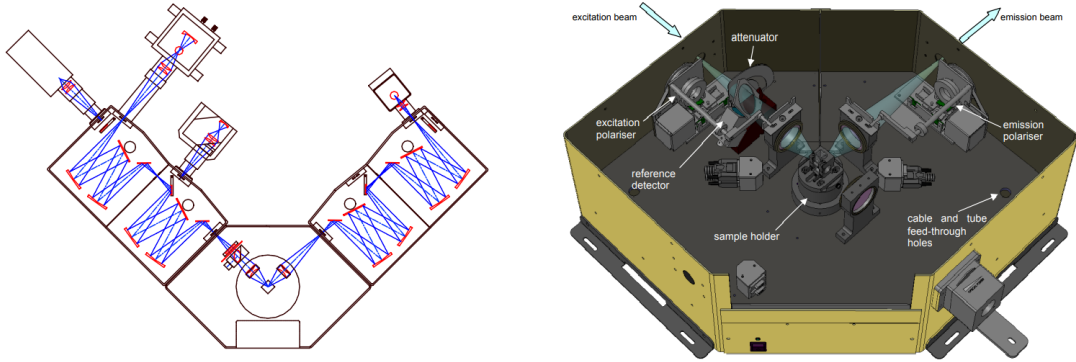


Figure 8: Used FLSP920 schemes of the layout (left), and sample chamber (right)

When using the diode laser as the excitation light source, the power can be adjusted by varying its intensity. Figure 9 displays the calibration graph of the 980 nm laser diode, depicting the relationship between the applied intensity and the output power. The threshold intensity is clearly visible on the graph, $i_{threshold} = 0.43$ A. This calibration was required for power-dependent emission spectra.

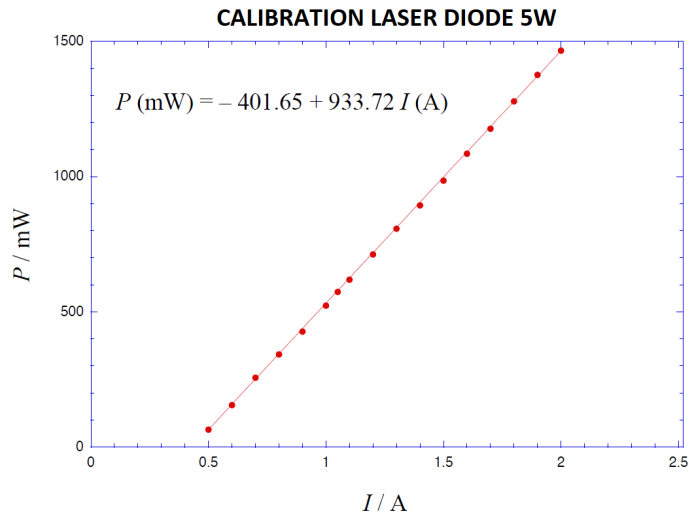
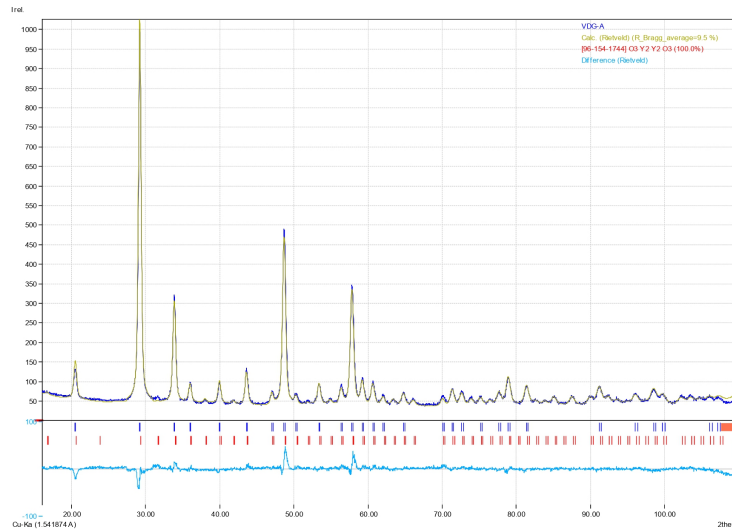


Figure 9: Relationship between current intensity and power of the diode laser used in the upconversion luminescence measurements.

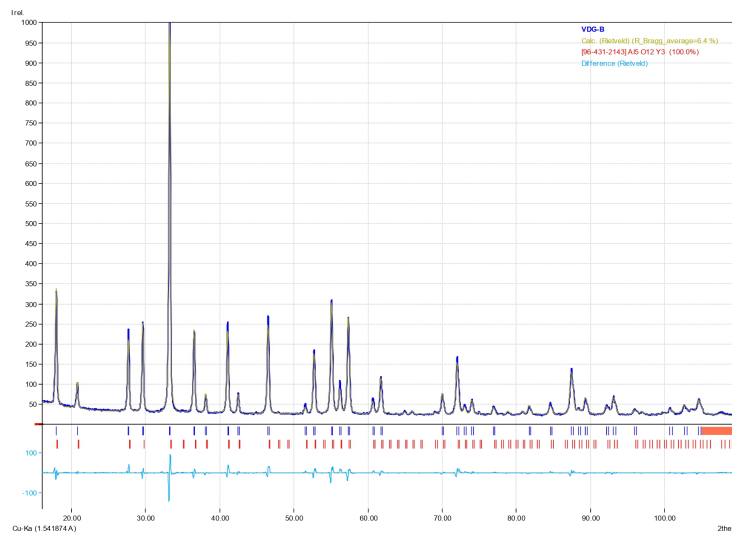
4 RESULTS AND DISCUSSION

4.1 Structural characterization

X-ray diffraction measurements and a further pattern matching analyses were applied to samples VDG-A, VDG-B, VDG-E, VDG-J and VDG-K (Figure 9a-e). Experimental data are represented with dark blue color. After a Rietveld Refinement, the calculated pattern is plotted in green. The peak positions of the principal phase obtained from the matching is showed with vertical red lines. If necessary, a second phase is used and showed with cyan vertical lines. The difference between the observed and calculated patterns is shown lower with a light blue line.

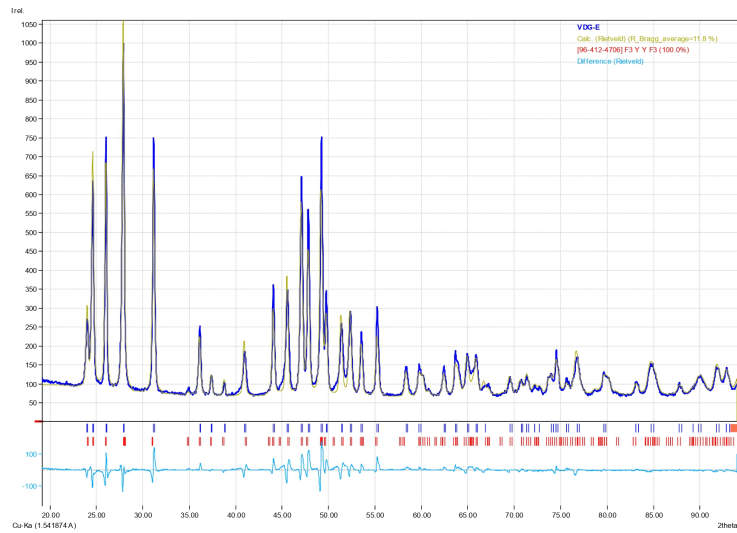


(a) XRD VDG-A (Y_2O_3)

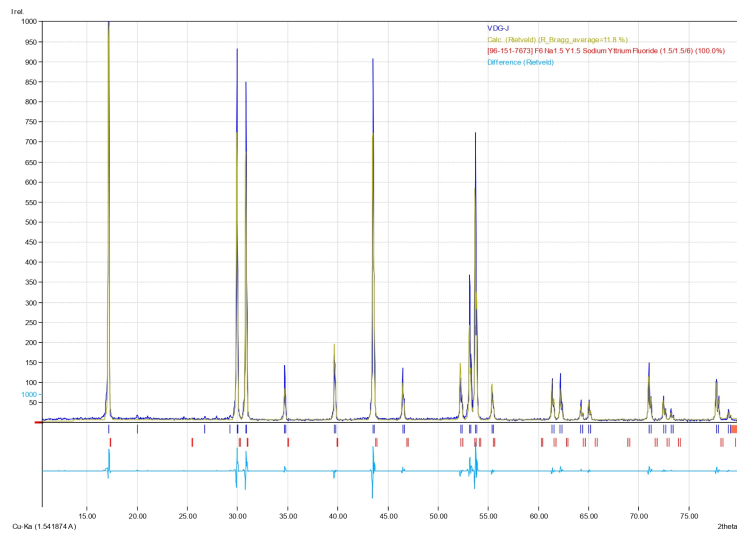


(b) XRD VDG-B (YAG)

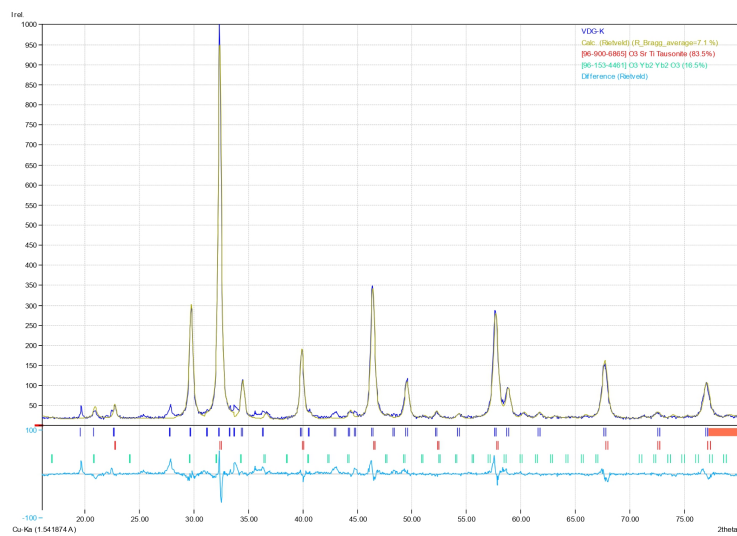
Figure 9: X ray diffraction patterns and pattern analysis.



(c) XRD VDG-E (YF_3).



(d) XRD VDG-J ($NaYF_4$)



(e) XRD $SrTiO_3$

Figure 9: X ray diffraction patterns and pattern analysis. (Cont.)

The analysis of XRD data shows that in all cases the synthesized samples matched the expected compound structures. In fact, the difference between the observed and calculated patterns remains fairly constant for all samples. Only sample VDG-K needed to take into consideration a second phase different from the expected one. However, this unexpected phase only accounted for around a 16% abundance in weight. It is fair to conclude that all samples were successfully synthesized. Table 2 collects the space groups and the lattice parameters of the most abundant phase obtained after a Rietveld refinement of the analyzed samples.

Table 2: XRD analyses results

Sample	VDG-A	VDG-B	VDG-E	VDG-J	VDG-K
Space group	I a -3 (206)	I a -3 d (230)	P n m a (62)	P -6 (174)	P m -3 m (221)
Cell parameters (refined) / Å	a = 10.5652	a = 12.0004	a = 6.3258 b = 6.8489 c = 4.4107	a = 5.9679 c = 3.5008	a = 3.9122

4.2 Spectroscopic characterization

Raman spectroscopy enables the study of molecular vibrations and provides insights into the structure and composition of samples. However, in certain cases, interpreting the results can become more complex due to the presence of luminescence phenomena, which can be mistaken for genuine Raman signals. It is necessary to consider an emission spectra in order to differentiate the Raman from the luminescence signal and, sometimes, use several excitation lines to gain further understanding of the results.

Raman spectra of VDG-A, VDG-B, VDG-F, VDG-J and VDG-K samples are collected in Figure 10. Since the assignment of Raman vibrational modes falls outside the scope of this work, and the quality of the obtained results is not high enough, only the information on the highest energy phonon has been collected and compared with the values from the literature in Table 3.

Table 3: Highest Raman energy phonon of the different host lattices studied in this thesis.

	Y ₂ O ₃	YAG	YF ₃	NaYF ₄	SrTiO ₃
Observed ω_{max} / cm ⁻¹	685	857	485	-	791
Bibliographic ω_{max} / cm ⁻¹	596 [25]	857 [26]	533 [27]	500 [28]	795 [29]

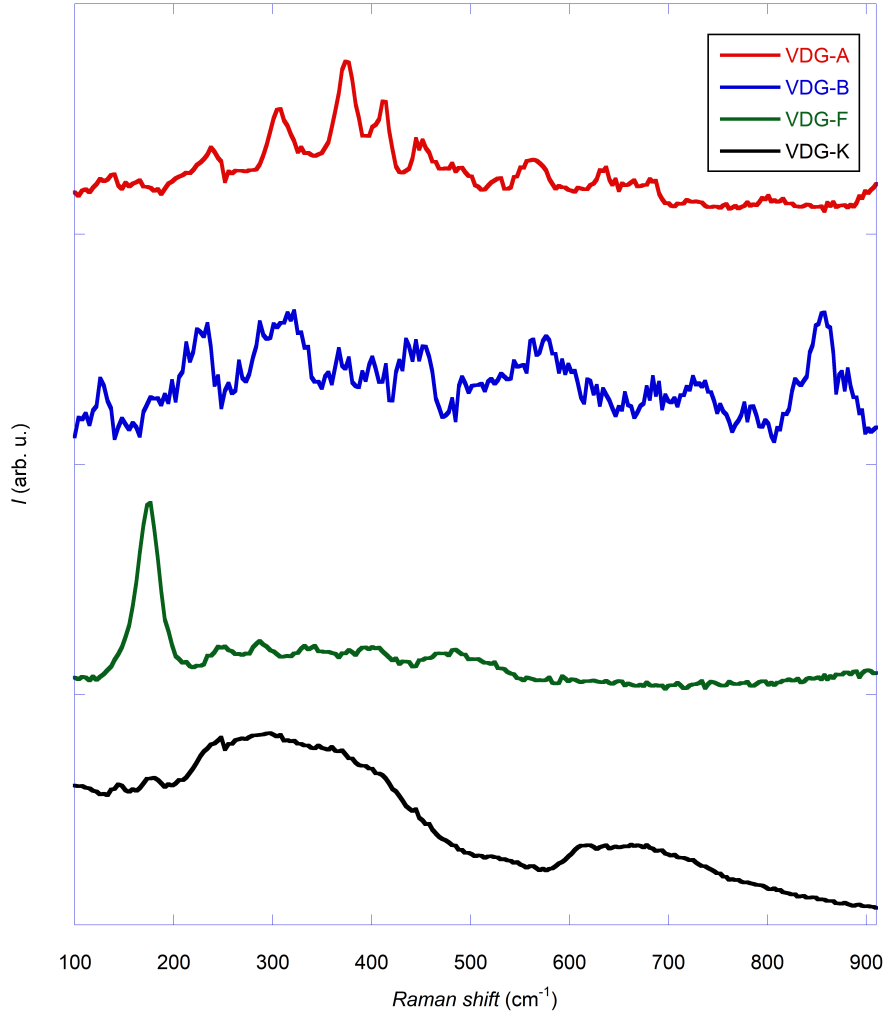


Figure 10: Raman spectra of VDG-A (red), VDG-B (blue), VDG-F (green), and VDG-K (black).

4.3 Diffuse Reflectance Spectroscopy

Figure 11 shows the absorbance spectra of samples VDG-A, VDG-B, VDG-E, VDG-J and VDG-K. Experimental peaks are labeled to absorption transitions using Dieke's diagram (Figure 2). Not all transitions present the same width and intensity. Since each sample corresponds to a different lattice, the crystal-field splitting may be slightly different, although the barycenter is pretty similar for all samples. Transitions of Er^{3+} take place from the $^4\text{I}_{15/2}$ ground state to higher energy levels. The transition of Yb^{3+} is related to the transition from the $^2\text{F}_{7/2}$ ground state to the $^2\text{F}_{5/2}$ excited state. Indeed this multiplets split by the crystal field and therefore the different peaks resolved in some samples correspond to transition between Stark levels of parent states.

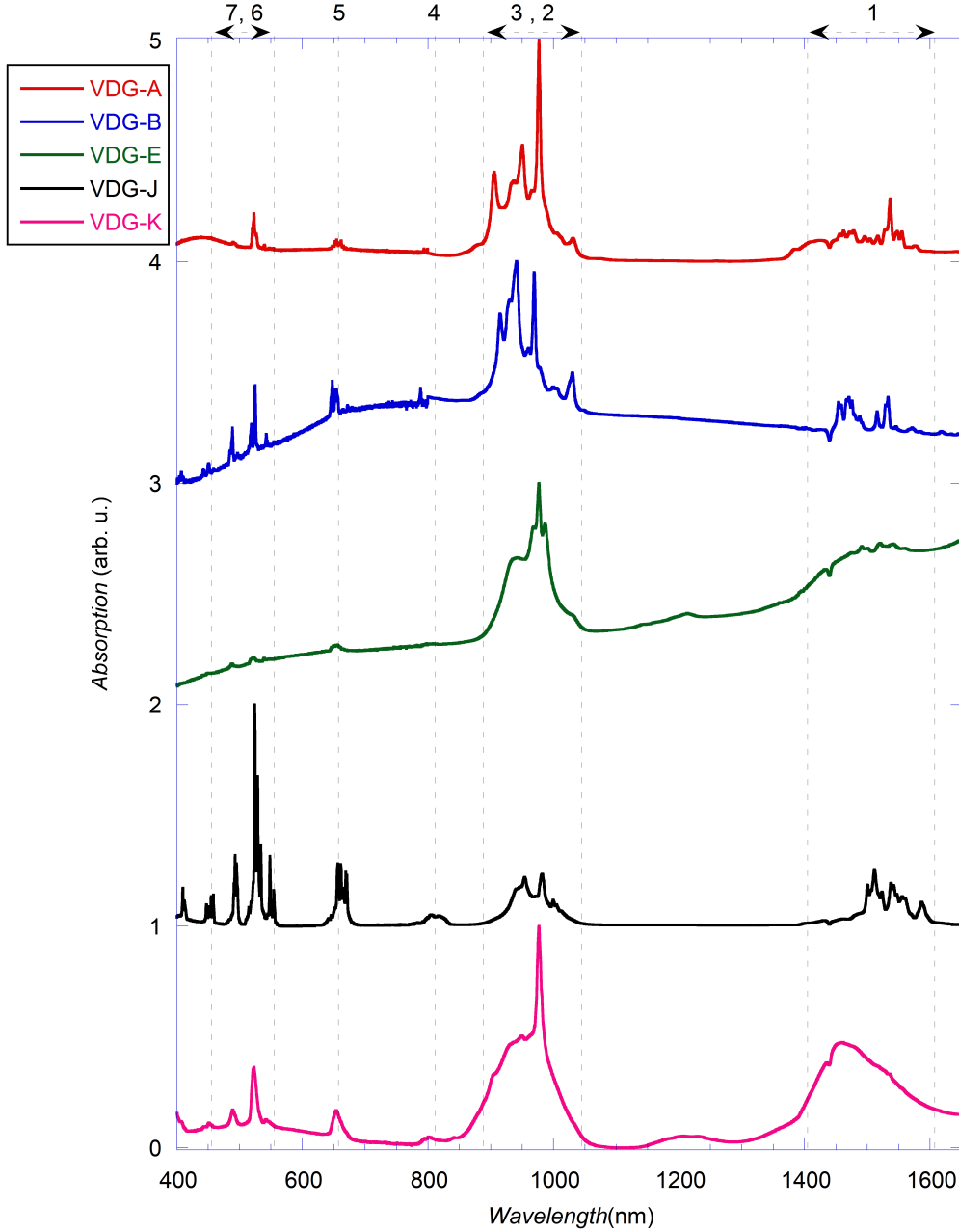


Figure 11: Absorption spectra of polycrystalline samples obtained from reflectance measurements.

Table 4 collects the assignment of each labelled peak from Figure 11 to a different transition, indicating the excited excited states.

Table 4: Assignment of the absorption spectra according to Dieke diagram.

Label	1	2	3	4	5	6	7
Ion	Er^{3+}	Yb^{3+}	Er^{3+}	Er^{3+}	Er^{3+}	Er^{3+}	Er^{3+}
Transition	${}^4\text{I}_{13/2}$	${}^2\text{F}_{5/2}$	${}^4\text{I}_{11/2}$	${}^4\text{I}_{9/2}$	${}^4\text{F}_{9/2}$	${}^5\text{S}_{3/2}$	${}^4\text{F}_{7/2}$
λ / nm	1400-1600	890-1050	890-1050	815	660	555-460	555-460

4.4 Fluorescence Spectroscopy

Dieke diagram (Fig. 2) was also used to make an estimation of the possibly observed transitions with fluorescence spectroscopy, and their emitting wavelengths. Figure 12 shows a diagram with the energy levels and the approximated wavelengths associated with different transitions, in order to later label the results.

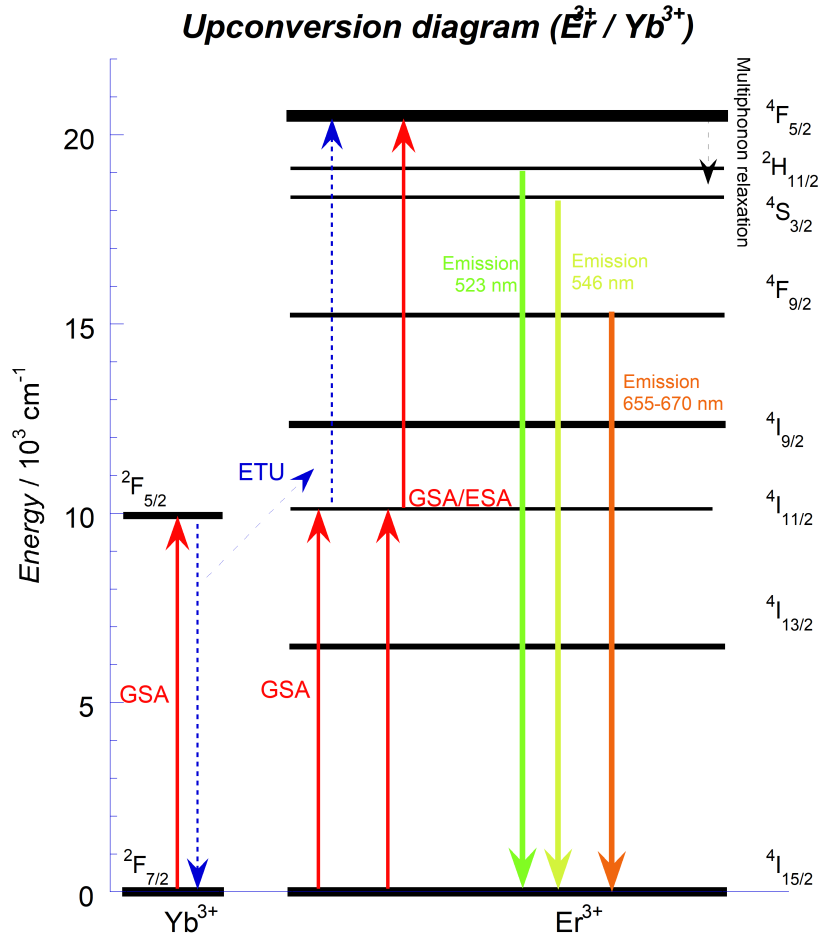


Figure 12: Energy level diagram and the upconversion mechanism

A 980 nm laser diode with the output power fixed to 532 mW was used as an excitation source to measure the emission between 500 and 700 nm for different samples with the same lattice (YF_3) while changing the concentration of Er and Yb. Figure 13 shows the as obtained results. In order to better visualize the dependence of the intensity ratios on the concentration, Figure 14 shows all the spectra normalized to the intensity of the peak at 538 nm.

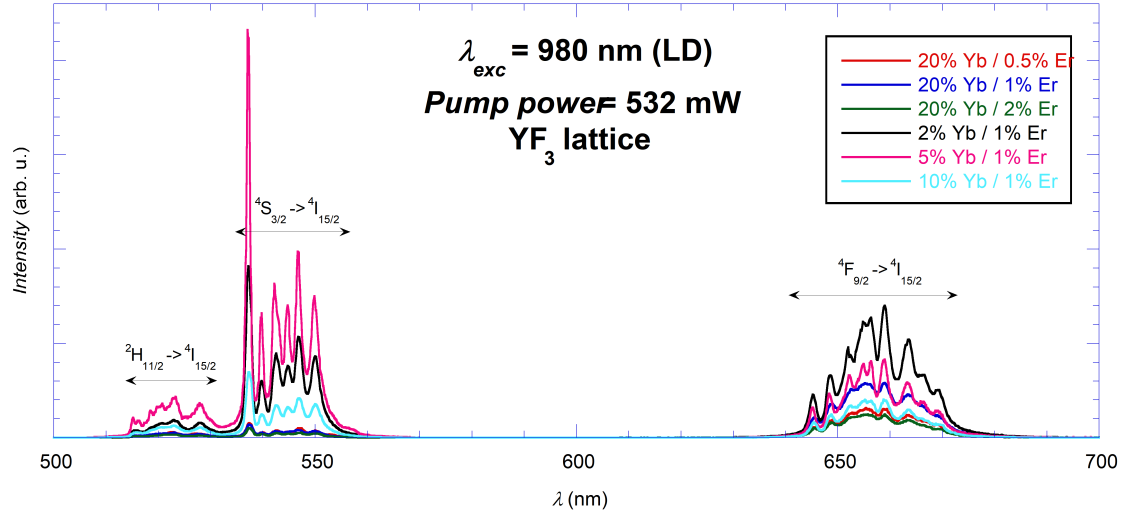


Figure 13: Upconversion emission scan (exc: 980 nm) for YF_3 doped in different concentrations. (See Table 1)

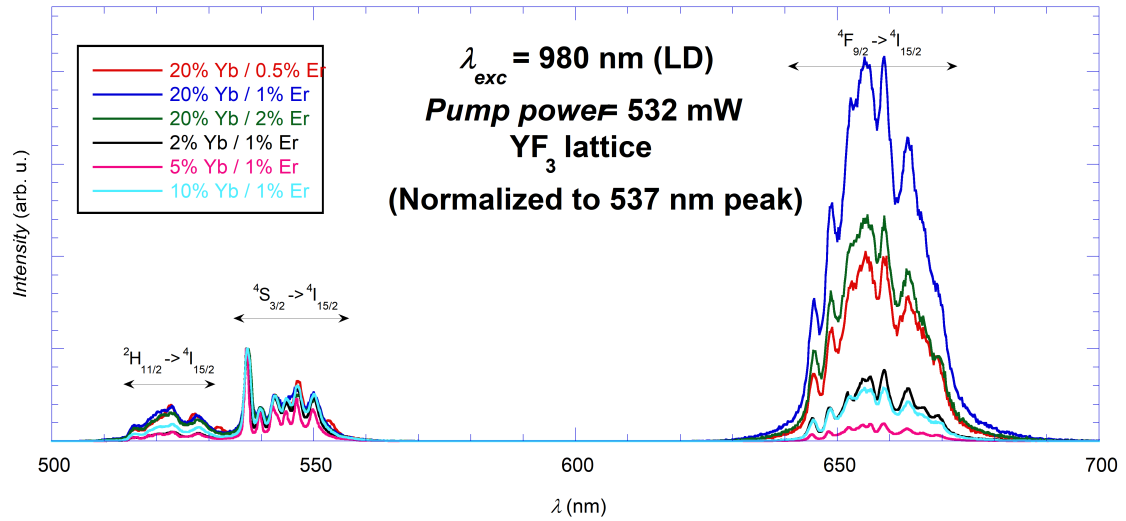


Figure 14: Normalized upconversion emission scan (exc: 980 nm) for YF_3 doped in different concentrations. (See Table 1)

Figures 13, 14 show how the emission intensity ratio of ${}^2\text{H}_{11/2} \rightarrow {}^4\text{I}_{15/2}$, ${}^4\text{S}_{3/2} \rightarrow {}^4\text{I}_{15/2}$, and ${}^4\text{F}_{9/2} \rightarrow {}^4\text{I}_{15/2}$ depends on the Yb / Er doping concentration. Figure 15 shows the green to red emission ratio (${}^2\text{H}_{11/2} \rightarrow {}^4\text{I}_{15/2} + {}^4\text{S}_{3/2} \rightarrow {}^4\text{I}_{15/2}$ over ${}^4\text{F}_{9/2} \rightarrow {}^4\text{I}_{15/2}$ integrated intensities) as a function of the RE doping concentrations.

From Fig. 15a, it can be obtained that the lowest green to red intensity ratio when using a 20% Yb concentration in a YF_3 lattice was when using 1% Er. On the other hand, when using a 1% Er concentration in a YF_3 lattice, the highest green to red ratio was achieved when using a 10% Yb concentration, as seen in Fig. 15b.

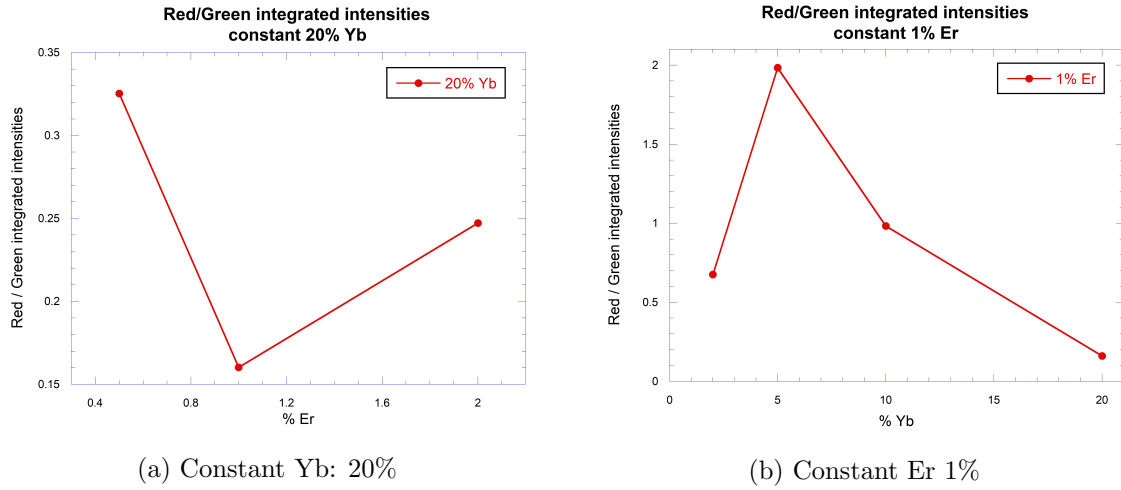


Figure 15: Green/Red ratio: RE^{3+} concentration dependence.

In the same manner, the 980 nm laser diode with the output power fixed to 532 mW was used as an excitation source to measure the emission between 500 and 700 nm for different samples, but maintaining the Er, Yb concentrations constant (2%, 20%) and varying the host lattices. Results are shown in Figure 16.

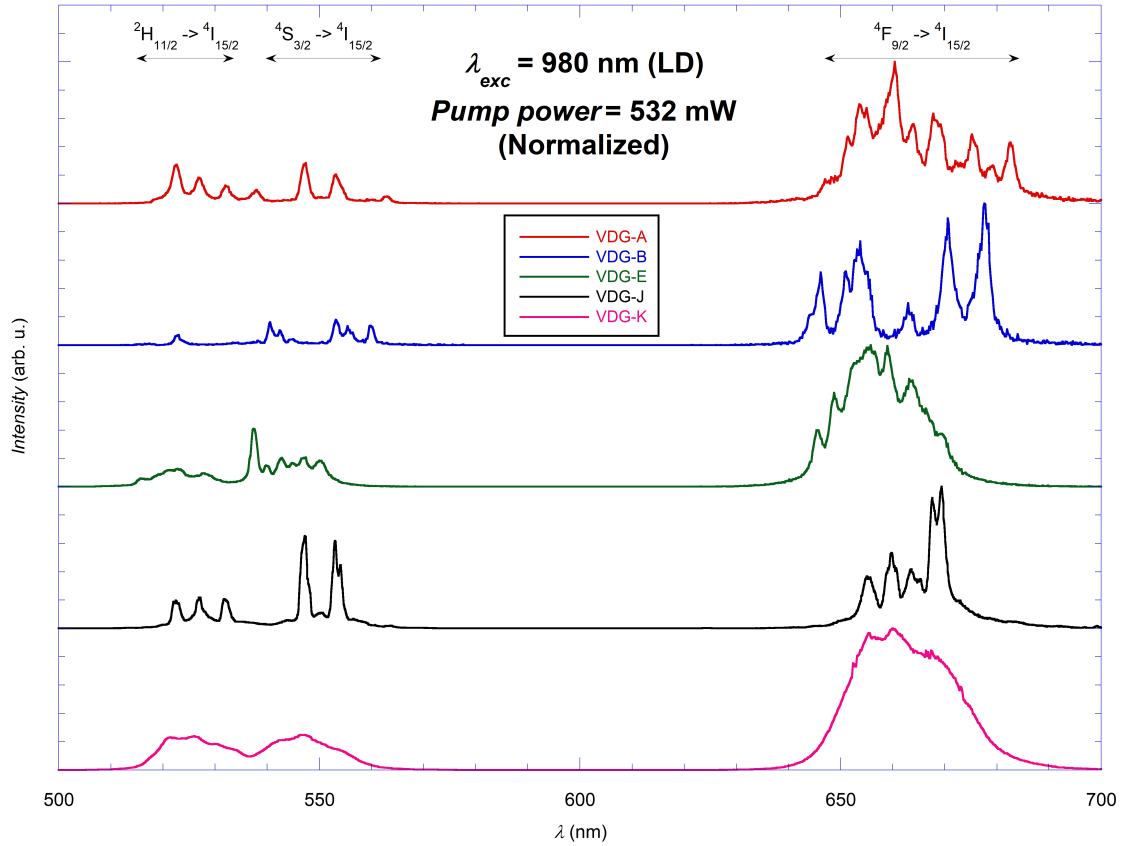


Figure 16: Upconversion emission scan (exc: 980 nm) for different lattices doped with 20% Yb and 2% Er.

Comparing Figures 14 and 16 it is possible to observe how the the RE concentration mainly affects the transitions intensities, but the host lattice also affects the bandwidth (Stark splitting due to different crystal field) and even slight changes in the emission wavelengths.

Also, emission scans varying the output power of the exciting source for samples with different lattices, but same dopant concentration, have been performed. While it was performed to samples VDG-A, VDG-B, VDG-E, VDG-J, and VDG-K, only the NaYF₄ case is shown to illustrate the results as an example in Figure 17.

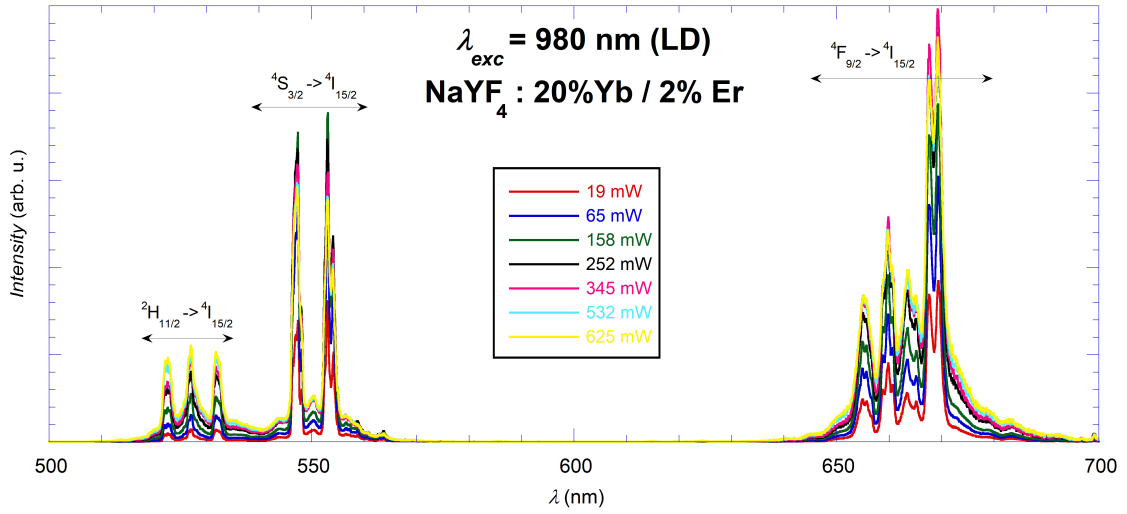


Figure 17: Upconversion emission scan (exc: 980 nm, varying output power) for different lattices doped with 20% Yb and 2% Er.

When obtaining the NaYF₄ measurements, after using a laser output power higher than 252 mW, the detectors would work with over one million counts per second. In these cases, the results may not be lineal, so a neutral density filter was used in the emission part of the chamber. Then, spectra with and without the filter where compared in order to adjust the results and make them comparable.

The next step was obtaining the integrated intensity (areas under the curve) of the red emission (Er³⁺: ${}^4F_{9/2} \rightarrow {}^4I_{15/2}$) for each lattice and excitation power used. Then, the natural logarithm of the calculated area was plotted against the natural logarithm of the laser output power. These results were successfully fitted to a linear function, indicating a power law. (See Figure 18).

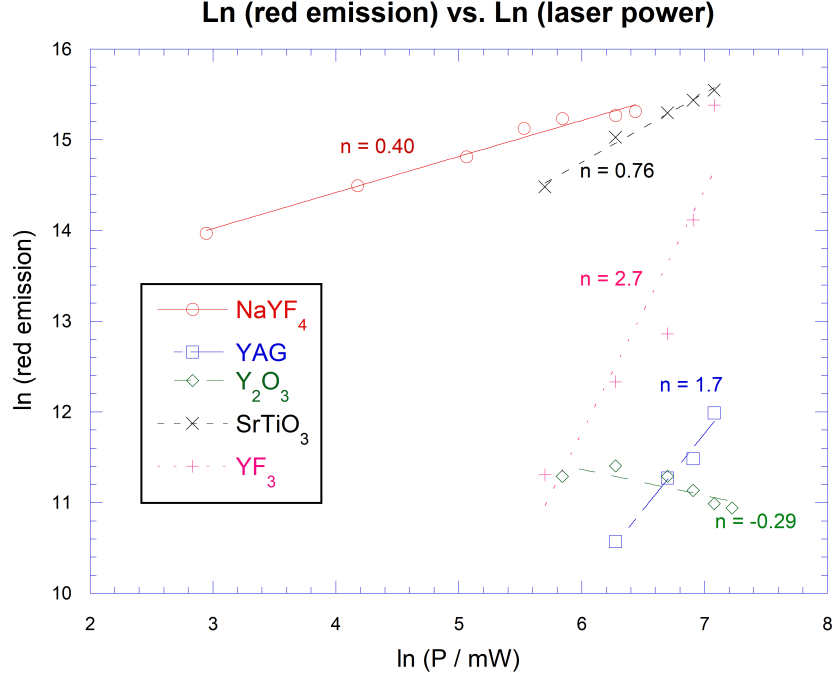
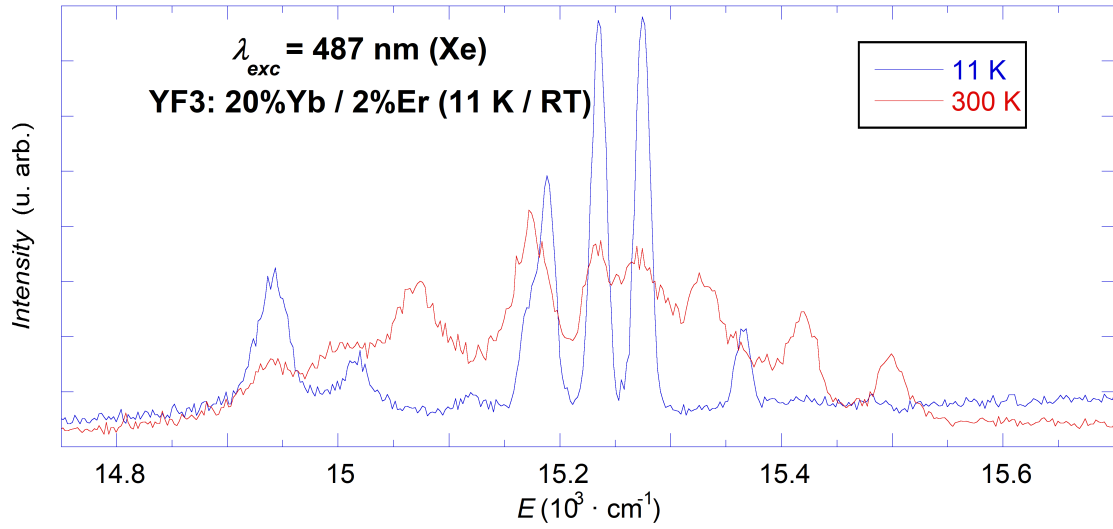
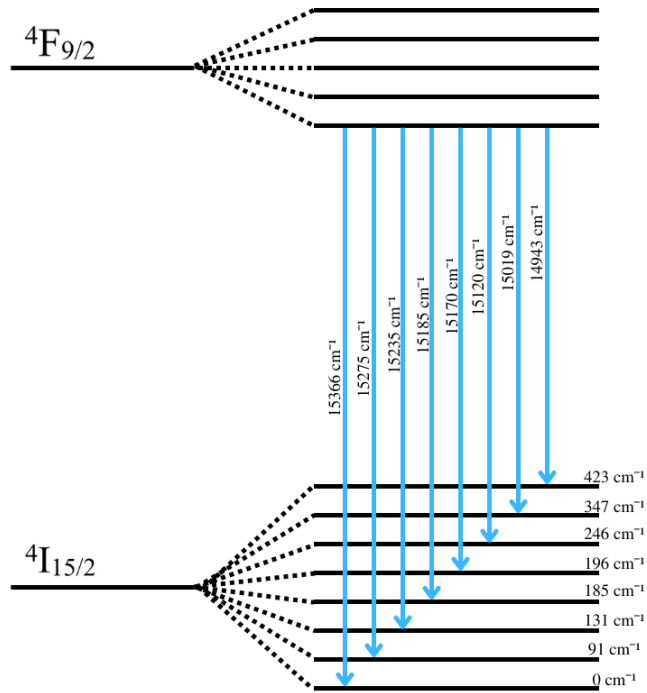


Figure 18: Integrated areas.

When the temperature of a sample decreases sufficiently, some of the Stark levels begin to depopulate, resulting in a lower number of bands that are also narrower. This allows for differentiation between the degeneracy due to the crystal-field effect. Measuring the distance between these bands allows for an estimation of the crystal-field splitting energy. Figure 19a shows an emission scan of the ${}^4F_{9/2} \rightarrow {}^4I_{15/2}$ transition at room temperature (red) and at 11 K (blue). At 11 K only the lowest energy Stark level is significantly populated, so we observe transition to all the Stark levels of the ground state. Since the degeneracy of ${}^4I_{15/2}$ is $J + 1/1$ (Kramer doublets) we expected 8 transitions, exactly what we observe. The energy difference between these transitions allows us to obtain a total crystal-field splitting of 423 cm^{-1} .



(a) Room temperature (red) and 11 K (blue) emission scan.



(b) Diagram of Fig. 19a process.

Figure 19: Green/Red ratio: RE concentration dependence.

5 CONCLUSIONS

X ray diffraction spectra showed how yttrium oxide, YAG and yttrium fluoride were successfully synthesized via homogeneous precipitation, sol-gel Pechini and hydrothermal method, respectively. The strontium titanate sample showed traces of other phases including Yb_2O_3 . All samples are able to accommodate RE^{3+} concentration up to a 100% by replacing the Y^{3+} ions.

The highest energy phonon of different host lattices were obtained using Raman spectroscopy, and then compared to the value obtained from different bibliographic sources, getting similar results.

Diffuse reflectance spectroscopy was used in order to obtain and compare the absorption spectra of different samples. Even when maintaining the RE dopant concentrations constant, different samples show different relative intensities, bandwidths and even a slight offset of the absorption transitions.

Upconversion Er / Yb concentration dependence has been studied. The emission wavelengths of the studied transitions did not depend on concentration changes. However, there was found to be a relation between the doping concentrations and the relative transition intensities. When doping a YF_3 lattice with 1% Erbium, green to red ratio of almost 1.98 achieved.

UC emission spectra varying the output power of the excitation laser for each studied sample has been measured. The natural logarithm of the red emission present (different) linear dependence(s) with the natural logarithm of the excitation laser power (of each lattice), indicating a power law between the upconversion transition intensity and the excitation power depending on the lattice.

References

- [1] Jean-Marie Tarascon. *Chemistry of Materials and Energy. Examples and Future of a Millennial Science: Inaugural Lecture delivered on Thursday 23 January 2014*. Collège de France, 2017.
- [2] C. Ronda. Rare-earth phosphors: Fundamentals and applications. In *Reference Module in Materials Science and Materials Engineering*. Elsevier, 2017.
- [3] Jun Yao, Cheng Huang, Chaohui Liu, and Mei Yang. Upconversion luminescence nanomaterials: A versatile platform for imaging, sensing, and therapy. *Talanta*, 208:120157, 2020.
- [4] John F. Porter. Fluorescence excitation by the absorption of two consecutive photons. *Phys. Rev. Lett.*, 7:414–415, Dec 1961.
- [5] François Auzel. Upconversion and anti-stokes processes with f and d ions in solids. *Chemical Reviews*, 104(1):139–174, 2004.
- [6] Richard Scheps. Upconversion laser processes. *Progress in Quantum Electronics*, 20(4):271–358, 1996.
- [7] Daniel R. Gamelin and Hans U. Gudel. *Upconversion Processes in Transition Metal and Rare Earth Metal Systems*. Springer Berlin Heidelberg, Berlin, Heidelberg, 2001.
- [8] Guanying Chen, Hailong Qiu, Paras N. Prasad, and Xiaoyuan Chen. Upconversion nanoparticles: Design, nanochemistry, and applications in theranostics. *Chemical Reviews*, 114(10):5161–5214, 2014.
- [9] Andrea Diego-Rucabado, M. T. Candela, F. Aguado, J. González, F. Rodríguez, R. Valiente, R. Martín-Rodríguez, and I. Cano. A comparative study on luminescence properties of Y_2O_3 : Pr^{3+} nanocrystals prepared by different synthesis methods. *Nanomaterials*, 10(8), 2020.
- [10] Karan Malhotra, David Hrovat, Balmiki Kumar, Grace Qu, Justin Van Houten, Reda Ahmed, Paul A. E. Piunno, Patrick T. Gunning, and Ulrich J. Krull. Lanthanide-doped upconversion nanoparticles: Exploring a treasure trove of nir-mediated emerging applications. *ACS Applied Materials & Interfaces*, 15(2):2499–2528, 2023.
- [11] Jing Zhou, Qian Liu, Wei Feng, Yun Sun, and Fuyou Li. Upconversion luminescent materials: Advances and applications. *Chemical Reviews*, 115(1):395–465, 2015.
- [12] V. Balaram. Rare earth elements: A review of applications, occurrence, exploration, analysis, recycling, and environmental impact. *Geoscience Frontiers*, 10(4):1285–1303, 2019.
- [13] Don L Anderson. *New theory of the Earth*. Cambridge University Press, 2007.

- [14] Miroslava Guricová, Jan Pinc, Juraĵ Malinĉik, Jakub Rak, Martin Kuchař, and Vilém Bartůněk. Rare earth nanofluorides: synthesis using ionic liquids. *Reviews in Inorganic Chemistry*, 39(2):77–90, 2019.
- [15] A. J. Freeman and R. E. Watson. Theoretical investigation of some magnetic and spectroscopic properties of rare-earth ions. *Phys. Rev.*, 127:2058–2075, Sep 1962.
- [16] G. H. Dieke and H. M. Crosswhite. The spectra of the doubly and triply ionized rare earths. *Appl. Opt.*, 2(7):675–686, Jul 1963.
- [17] Marta Quintanilla Morales. *Caracterización espectroscópica y aplicaciones de la conversión infrarrojo-visible en LiNbO₃ y YF₃ activados con iones Tm³⁺ y Er³⁺*. PhD thesis, Universidad de Cantabria, 2010. Tesis doctoral inédita. Fecha de lectura: 22-10-2010.
- [18] L. A. Riseberg and H. W. Moos. Multiphonon orbit-lattice relaxation of excited states of rare-earth ions in crystals. *Phys. Rev.*, 174:429–438, Oct 1968.
- [19] J. Freek Suijver. *Upconversion Phosphors*, chapter 6, pages 133–177. John Wiley & Sons, Ltd, 2007.
- [20] K. W. Krämer, D. Biner, G. Frei, H. U. Güdel, M. P. Hehlen, and S. R. Lüthi. Hexagonal sodium yttrium fluoride based green and blue emitting upconversion phosphors. *Chemistry of Materials*, 16(7):1244–1251, 2004.
- [21] J. Taboada Gutiérrez. Synthesis, characterization and optical properties of nanoparticles of strontium titanate doped with rare earths. Master’s thesis, Universidad de Cantabria, 7 2017.
- [22] S.A. Hassanzadeh-Tabrizi. Synthesis and luminescence properties of yag: Ce nanopowder prepared by the pechini method. *Advanced Powder Technology*, 23(3):324–327, 2012.
- [23] R. de L. Kronig. On the theory of dispersion of x-rays. *J. Opt. Soc. Am.*, 12(6):547–557, Jun 1926.
- [24] KRAMERS H. A. La diffusion de la lumiere par les atomes. *Atti Cong. Intern. Fisica (Transactions of Volta Centenary Congress) Como*, 2:545–557, 1927.
- [25] G. Skandan, C.M. Foster, H. Frase, M.N. Ali, J.C. Parker, and H. Hahn. ”phase characterization and stabilization due to grain size effects of nanostructured y₂o₃”. *Nanostructured Materials*, 1(4):313–322, 1992.
- [26] S. Kostić, Z.Ž. Lazarević, V. Radojević, A. Milutinović, M. Romčević, N.Ž. Romčević, and A. Valčić. Study of structural and optical properties of yag and nd:yag single crystals. *Materials Research Bulletin*, 63:80–87, 2015.
- [27] W. R. Wilmarth, G. M. Begun, S. E. Nave, and J. R. Peterson. The Raman spectra of polycrystalline orthorhombic YF₃, SmF₃, HoF₃, YbF₃, and single crystal TbF₃. *The Journal of Chemical Physics*, 89(2):711–715, 07 1988.

- [28] C. Renero-Lecuna, R. Martín-Rodríguez, R. Valiente, J. González, F. Rodríguez, K. W. Krämer, and H. U. Güdel. Origin of the High Upconversion Green Luminescence Efficiency in $NaYF_4 : 2\%Er^{3+}, 20\%Yb^{3+}$. *Chemistry of Materials*, 23(15):3442–3448, 2011.
- [29] Federico A. Rabuffetti, Hack-Sung Kim, James A. Enterkin, Yingmin Wang, Courtney H. Lanier, Laurence D. Marks, Kenneth R. Poeppelmeier, and Peter C. Stair. Synthesis-dependent first-order raman scattering in $srTiO_3$ nanocubes at room temperature. *Chemistry of Materials*, 20(17):5628–5635, 2008.